

## Spontaneous Anchoring-Mediated Topography of an Orientable Fluid

Andrew J. Ferris<sup>1,\*</sup>, Charles Rosenblatt<sup>1</sup>, and Timothy J. Atherton<sup>2</sup>

<sup>1</sup>*Department of Physics, Case Western Reserve University, Cleveland, Ohio 44106, USA*

<sup>2</sup>*Department of Physics, Tufts University, Medford, Massachusetts 02155, USA*

(Received 14 August 2020; accepted 13 January 2021; published 4 February 2021)

A topography in a Newtonian fluid occurs if there is a disturbance near the surface. But what if there is no such disturbance? We show by optical profilometry that a thin nematic film resting on a topological-defect-patterned substrate can exhibit a hill or divot at the opposing free (air) interface in the absence of a topological disturbance at that interface. We propose a model that incorporates several material properties and that predicts the major experimental features. This work demonstrates the importance of, in particular, anisotropic surface interactions in the creation of a free-surface topography.

DOI: 10.1103/PhysRevLett.126.057803

Freely flowing Newtonian fluids are, in general, unable to support an equilibrium topography at an interface with another fluid. Nevertheless, there has been an ongoing effort to find counterexamples. Under certain conditions it is known that an orientable Newtonian fluid, examples of which are nematic (but not smectic [1]) liquid crystals (LCs), certain polymers, and aqueous mixtures of tobacco mosaic virus, can support a topography when there is a disturbance near the interface. This can occur, for example, with small anisometric structures such as vesicles and tactoids [2–6], inclusions or defects residing at the free surface [7–10], or topological defects (TDs) that completely traverse the fluid film's thickness and that have reached the air interface. Such TDs can be pinned to the solid substrate as, observed by Virga and Schadt [11,12], or associated with mismatched boundary conditions in a chiral nematic LC [13,14]. But it is surprising that an orientable Newtonian fluid can possess an equilibrium free-surface topography in the absence of a disturbance at or near that surface. Why should this be? What sort of long-range interactions could induce an “action-at-a-distance” [15] variation in the free-surface topography?

In this Letter we show experimentally and theoretically that a topological defect of strength  $m = +1$  (a so-called “boojum”) localized at the underlying substrate in a nematic LC can create a topography at the opposing nematic LC-air interface in the absence of any singularity traversing the film. Our “hybrid” boundary conditions (nominally planar at the substrate and vertical at the air interface) result in a topography at the fluid-air interface based on a trade-off among elasticity, the isotropic component of the surface energy (surface tension), and its anisotropic part (anchoring), providing the first equilibrium topography of a Newtonian fluid in the absence of a singularity at the perturbed free surface and that is based solely on the material properties of the film and its interfaces.

Experimental details are described in Supplemental Material [16,17]. A sample was prepared by AFM scribing a TD pattern of strength  $m = +1$ ,  $\varphi = 0^\circ$  (radial) having a “confinement radius”  $\ell$  on a polymer-coated substrate [18]. A thin layer of liquid crystal 8CB was then spin coated on the substrate. The LC's free-surface topography was measured by optical profilometry.

Figure 1(a) shows a 3D reconstruction of the surface profile of the LC-air interface for film thickness  $d = 610 \pm 30$  nm above an underlying  $m = +1$ ,  $\varphi = 0^\circ$  (radially) patterned surface. Immediately visible is a hill-like protrusion rising above a nearly flat nematic surface. Reflecting the underlying pattern, the hill is azimuthally

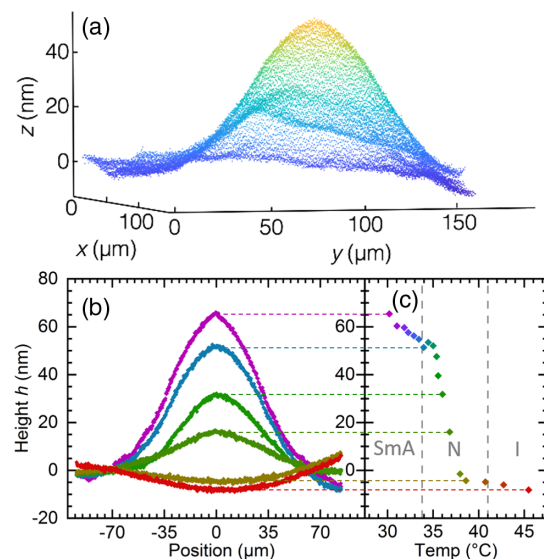


FIG. 1. (a) Experimental 3D scatter plot of topography at the LC-air interface induced by an underlying TD at the substrate. (b) Height profile change at selected temperatures. (c) Peak height  $h$  versus temperature, showing transition temperatures  $T_{NA}$  and  $T_{NI}$ .

symmetric, and its height  $h$  above the background increases monotonically toward  $r = 0$ , reaching a peak height  $h = 52 \pm 4$  nm. This corresponds to 9% of the film's total thickness. (Note that we have observed  $h/d$  as large as 0.21 in the nematic phase.)

The height distribution  $h(r)$  changes significantly with temperature [Fig. 1(b)]. It is virtually flat above the  $NI$  transition temperature  $T_{NI} \sim 41^\circ\text{C}$ , with a tiny divot observed in Fig. 1(b) (in this sample only) due to a dust particle beyond  $r = \ell$ . A small hill becomes visible at the core after cooling below  $T_{NI}$ . This hill grows in height as we cool further into the nematic, which is our focus. Figure 1(c) shows the peak height  $h$  versus temperature, including the pretransitional behavior on approaching the nematic to Smectic-A (SmA) transition temperature. Although effects in the SmA phase are beyond the scope of the current work and will be published elsewhere, we note several features specific to the SmA phase and distinct from the nematic: formation of *curved* oily streak defects [2] transverse to the patterned easy axis; significant transfer of LC to beyond the patterned region with a hill rising above the patterned region, all of which is now depressed from the surrounding area; and an extremely sharp cone whose apex height ( $66 \pm 5$  nm) now reaches 10% of the film's asymptotic thickness. These smectic cones have been observed with absolute heights as large as  $h = 200$  nm (for  $d = 1200$  nm) and relative heights as large as 65% ( $h = 50$  nm,  $d = 75$  nm).

Returning to nematic films, the height, shape, and even the sign of the topography are found to depend on the film thickness  $d$ : Thinner films exhibit taller hills as a fraction of the film thickness, with  $h$  generally decreasing with increasing film thickness. Additionally, for thinner films ( $d \sim 100$  nm), we observe that hills are more likely to have a domelike (rather than cusplike) shape [Fig. 2(a)], but become more conical with a singularity at the peak for thicker films [ $\sim 600$  nm, Figs. 2(b) and 2(c)]. For the domelike topography, its rounded shape in conjunction with the vertical boundary conditions at the air interface ensure that variations in the director at the substrate smooth out rapidly with increasing  $z$ . Thus, no disclination line projects from the patterned surface defect through the LC to the top surface. This behavior is due to an energy balance and is borne out by our modeling below. Thus, the domelike behavior indicates the presence of a boojum at the patterned surface, and that the free-surface topography is not generated by a local surface defect or transmitted by a bulk disclination line—this is unlike the case reported in Refs. [11–14]. Instead, the topography is mediated through anchoring, as well as elastic forces from the patterned substrate to the free surface. We also note that the height of the hill also depends on  $\ell$ , the distance out to which the radial ( $m = +1$ ,  $\varphi = 0^\circ$ ) TD is patterned:  $h$  increases monotonically with pattern diameter  $2\ell$  in the SmA phase ( $h = 8, 10$ , and  $14 \pm 2$  nm for  $\ell = 15, 25$ , and  $35 \mu\text{m}$ , respectively for  $d = 500 \pm 20$  nm just below  $T_{NA}$ ), with

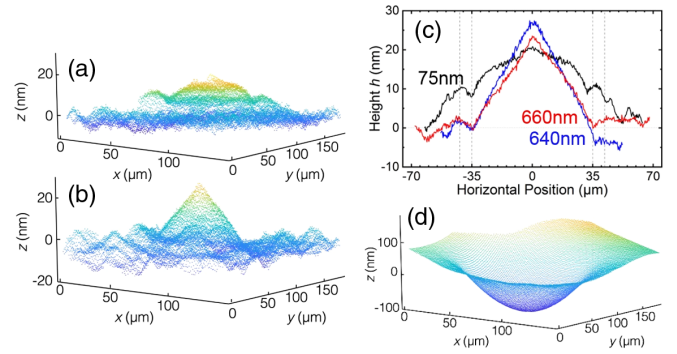


FIG. 2. (a) Domelike behavior for a film of thickness  $d = 75$  nm. (b) Conelike topography for  $d = 660$  nm film on the same patterned substrate. (c) Profiles of slices through the core of the same physical sample at several different thicknesses. The extent of the two inner vertical lines corresponds to the  $2\ell = 70 \mu\text{m}$  radially patterned diameter, and the two outer vertical lines to the full  $85 \mu\text{m}$  patterned square. (d) Image of a divot for  $d = 1030$  nm film.

similar but smaller (and thus noisy) results in the nematic phase as well. Finally, Fig. 2(d) shows a divot.

We also compared our nematic results to a region of the same substrate that had been patterned with an underlying  $m = +1$ ,  $\varphi = \pi/2$  topological defect—this corresponds to an alignment pattern of concentric circles. This pattern exhibits no significant topography, suggesting that the source of the topography is not simply elastic relaxation near the core—indeed, both the radial and concentric circle patterns have the same total 2D elastic energy density (in the single elastic constant approximation) at the defect core.

We examine the three major terms of the free energy: surface tension, elastic forces, and anchoring. In both the radial and concentric circle geometries, surface tension at the free surface tends to minimize curvature, promoting a uniformly flat topography [Fig. 3(a)]. Next are elastic forces, with the director constrained (nearly) normal to the free surface. Focusing on the radial easy axis pattern, very close to  $r = 0$  the director must melt, become biaxial [19–21] when tightly confined in specific geometries [22–24], a condition that is not met in our experiments, or become vertically aligned at the substrate. The latter scenario is effectively the common escaped radial configuration [25,26] and is consistent with our setup. For the latter case the far-field region beyond  $r > \ell$  finds its polar orientation  $\theta$  undergoing a bend or splay distortion along the  $z$  axis to meet the hybrid-alignment boundary conditions. The total energy of this far-field region can be reduced by increasing the local film thickness to spread the distortion over a larger  $z$  distance. With a constant volume constraint, material must be transported away from the core region near  $r = 0$ , thus promoting a divot for both configurations [Figs. 2(d) and 3(b)]. We note that these nematic divots derive from very different physics than those in the SmA phase [27,28].

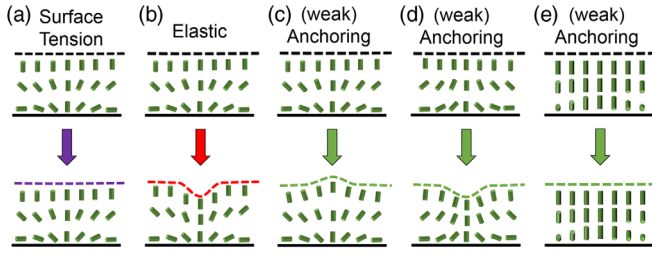


FIG. 3. Illustration visualizing the resulting topography from the energy contributions of (a) surface tension promotes flatness, (b) elastic forces promote divots, (c),(d) underlying splay in the weak-anchoring regime for both senses of director escape, the first promoting hills and the second divots, and (e) underlying twist in the weak-anchoring regime promoting neither hills nor divots.

The third term, anchoring, is the source of the hill-like behavior [Fig. 3(c)] for the radial pattern. Because of the hybrid boundary conditions, there is a director torque at the surfaces, and the LC must be pretilted slightly, by angle  $\theta_f(r)$ , from the normal at the free surface (vanishing as  $r \rightarrow 0$ ). This pretilt anchoring cost can be mitigated by a deformation of the free surface to form a hill [Fig. 3(c)] or a divot [Fig. 3(d)], depending on the sense of pretilt at the substrate. Figure 3(e) shows the case of a concentric circle easy axis pattern, with a twist distortion along an axis passing through  $r = 0$  at the substrate. Elastic energy relaxation requires that  $\nabla h$  be azimuthal, although owing to azimuthal symmetry  $\nabla h = 0$ . Thus free-surface anchoring promotes neither hill nor divot, leaving elasticity as the main driving force for the topography. That the topography is negligible for  $m = +1$ ,  $\varphi = \pi/2$  [Fig. 3(e)] suggests that the elastic forces are weak.

The relative trade-off among the three energy contributions determines the magnitude of  $h$  and its sign. We observed the pretilt phenomenon experimentally, wherein heating and cooling through  $T_{NI}$  randomly nucleates the sense of pretilt—this is due to the bidirectional scribing—thereby interchanging hill and divot. We note that scribing the patterns unidirectionally predisposes one sense of substrate pretilt, with hills for radially inward scribing and divots for outward scribing. Thus, the shape of the topography depends on force balance, with anchoring typically dominating. This, in turn, depends on the LC’s materials parameters, the scribing pattern, the scribing radius  $\ell$ , and the film thickness  $d$ .

We now turn to an overview of the modeling with a patterned defect at the substrate; a more extensive exposition will be published elsewhere. The free energy of the system consists of the usual surface tension, elastic, and anchoring contributions,

$$F = \frac{1}{2} \int_{\Omega} f(\mathbf{n}, \nabla \mathbf{n}) dV + \int_{\partial\Omega} \left[ \sigma - \frac{W}{2} (\mathbf{n} \cdot \mathbf{n}_e)^2 \right] dA, \quad (1)$$

where  $\sigma$  is the surface tension, the elastic contribution is  $f = K_{11}(\nabla \cdot \mathbf{n})^2 + K_{22}(\mathbf{n} \cdot \nabla \times \mathbf{n})^2 + K_{33}|\mathbf{n} \times \nabla \times \mathbf{n}|^2$ ,  $K_{11} = K_{22} = K_{33} = K$  are the splay, twist, and bend elastic constants in the equal constant approximation, and  $W$  is the anchoring strength coefficient. The second integral is taken over the free surface with the director  $\mathbf{n}$  fixed at the lower substrate.

Two length scales,  $\zeta = K/\sigma$  and  $\xi = K/W$ , characterize the relative influence of the three terms. Far above the  $N$ -SmA transition, approximate values for these are  $\zeta \sim 0.4 \ll \xi \lesssim 100$  nm; hence the upper surface remains flat and the director adopts the configuration in Fig. 3(a). Note that the director deviates slightly from vertical above the pattern due to the finite anchoring strength. As the temperature cools towards the  $N$ -SmA transition, two effects occur: First,  $K_{22}$  and  $K_{33}$  diverge [29]; second, the SmA phase grows inward from the substrate [30], enhancing surface order and, importantly, increasing the surface anchoring  $W$  [31,32]. This tends to enhance  $h$  for both hills and divots on nearing  $T_{NA}$ .

Now suppose the free interface can vary. The surface tension term in Eq. (1) resists deformations [Fig. 3(a)]. Elastic stresses tend to push the interface upward to mitigate  $d\theta/dz$ : As described above, this leaves a divot near  $r = 0$ , where  $d\theta/dz = 0$  [Fig. 3(b)]. The anchoring term requires careful consideration: It is typically thought to promote alignment of the director with respect to a fixed easy axis  $\mathbf{n}_e$  defined relative to the surface normal. Here we reverse the causality and investigate how a spatially changing  $\mathbf{n}$  can induce variations in  $\mathbf{n}_e$  and hence the topography of the surface.

To do so, the free surface is parametrized in dimensionless (scaled by  $d$ ) cylindrical coordinates  $(\rho, u, Z)$  as  $\mathbf{X} = \{\rho, u, H(\rho)\}$  and, hence, the surface normal is  $\hat{\mathbf{s}} = \{-H'(\rho), 0, 1\}/[1 + H'(\rho)^2]$ . Here,  $H = h/d$ ,  $L = \ell/d$ , and the prime denotes  $\partial/\partial R$ . Similarly, the director at the surface is parametrized to lie at a constant azimuthal angle  $\phi$  to the radial direction,  $\mathbf{n} \equiv \{n_\rho, n_u, n_z\} = \{\sin(\theta(\rho)) \cos \phi, \sin(\theta(\rho)) \sin \phi, \cos(\theta(\rho))\}$ . Hence, the anchoring term in Eq. (1) becomes

$$F_w = -\pi W d \int_0^L \frac{[\cos \theta(\rho) - H'(\rho) \cos \phi \sin \theta(\rho)]^2}{\sqrt{1 + H'(\rho)^2}} \rho d\rho, \quad (2)$$

revealing a coupling between topography  $H'(\rho)$  and orientation  $\theta(\rho)$ . Notice that the coupling vanishes if  $\theta = 0$ , where the director is vertical, and similarly if  $\phi = \pi/2$ , where the director is azimuthal; here a spatially varying director does not induce topography.

Experimentally,  $H \ll 1$ , suggesting a perturbative approach. We therefore series expand about a solution where the director is nearly vertical at the free surface and fixed by elasticity,  $\theta \approx \alpha \theta_1(\rho)$ , and the interface is nearly flat,  $H(\rho) \approx \alpha H_1$ , where  $\alpha$  is an expansion parameter. We include the surface tension,

$$F_\sigma = 2\pi\sigma d \int_0^L \sqrt{1 + H'(\rho)^2} \rho d\rho,$$

and a volume constraint  $2\pi\lambda d \int_0^L H(\rho)\rho d\rho$ , but neglect the elastic stress, as this has leading order  $\alpha^3$  while the other terms are of order  $\alpha^2$ . With these considerations, the linearized Euler-Lagrange equation is obtained,

$$(1+w)(H'_1 + \rho H''_1) + 2w \cos \phi(\theta_1 + \rho\theta'_1) + \lambda\rho = 0, \quad (3)$$

where  $w = W/\sigma$ . A suitable ansatz for  $\theta_1$  is  $\theta_1 = (\pi/2) \tanh(\pi\rho/2)/(1+\Gamma)$ , where  $\Gamma = Wd/K$ . Inserting this into Eq. (3), we obtain a solution:

$$H(R) = H_0 - \frac{\lambda\rho^2}{2\pi(1+w)} - \frac{2w \cos \phi \log[\cosh(\pi\rho/2)]}{(1+w)(1+\Gamma)}. \quad (4)$$

The constants  $\lambda$  and  $H_0$  are determined by imposing the boundary condition  $H'(L) = 0$  and volume constraint  $\int_0^L H(\rho)\rho d\rho = 0$ . From the solution [Eq. (4)], the magnitude of the dimensionless topography  $\Delta H \equiv H(L) - H(0)$  may be estimated,

$$\Delta H = \frac{w \cos \phi \{4 \log[\cosh(\pi L/2)] - \pi L \tanh(\pi L/2)\}}{2(1+w)(1+\Gamma)},$$

and solutions are plotted in Fig. 4(a) for different  $L$ . The profile becomes increasingly conical with increasing  $L$ . Thus, we have the following takeaways: (i) our analytic model articulates the mechanism(s) for the topography, (ii) it predicts that a topography is observed only for the case of a radial surface pattern, consistent with experiment, and (iii) it predicts that the topography scales with confinement distance  $L$ , also consistent with observation.

We also perform numerical simulations relaxing the strong assumptions of the above model. The full free energy [Eq. (1)] with three elastic constants is minimized subject to a volume constraint both with respect to the director and the shape of the domain using one of the authors MORPHO code of DeBenedictis and Atherton [33]; an initial 2D rectangular domain is used and all quantities are represented using linear interpolation on a triangular finite element mesh. The height is fixed at  $\rho = L$  on the right-hand boundary. A typical height profile is displayed in Fig. 4(b) and closely resembles those from the analytical model despite the much less restrictive assumptions of the calculation. Additionally, we display the normal component of the generalized force  $(\partial F/\partial x_i) \cdot \hat{s}$  on the  $i$ th boundary vertex due to the respective terms [Fig. 4(c)].

To summarize, we have shown experimentally and theoretically that the topography of a nematic LC, i.e., an orientable Newtonian fluid, at an air interface can be determined by the easy axis pattern of the underlying substrate. The interplay of surface tension, elasticity, and especially anchoring alone determines the shape of

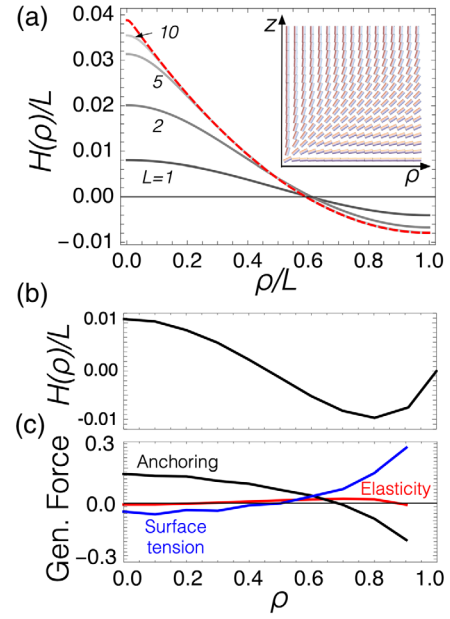


FIG. 4. a) Illustration of flat interface solution (inset) and analytical height profile for different  $L$ ;  $w = 0.1$ ,  $\Gamma = 10$ ,  $\phi = 0$ . Asymptotic solution for  $L \rightarrow \infty$  is shown in red for comparison. (b) Numerically minimized height profile with finite elements. (c) Generalized forces on the boundary vertices due to different terms in the elastic energy.

the free-surface topography, without the need of a singular defect running from the substrate to the air interface.

We thank Professor Robin Selinger, Professor Nigel Mottram, Professor Emmanuelle Lacaze, and Professor Samo Kralj for useful discussions. Support came from the NSF under Grants No. DMR1901797 (A. J. F. and C. R.) and No. DMR1654283 (T. J. A.).

\*Present address: Sandia National Laboratory, Albuquerque, New Mexico 87123, USA.

- [1] M. P. Mahajan, M. Tsige, P. L. Taylor, and C. Rosenblatt, *Phys. Fluids* **11**, 491 (1999).
- [2] F. C. MacKintosh and T. C. Lubensky, *Phys. Rev. Lett.* **67**, 1169 (1991).
- [3] Y. K. Kim, S. V. Shiyankovskii, and O. D. Lavrentovich, *J. Phys. Condens. Matter* **25**, 404202 (2013).
- [4] Z. Dogic and S. Fraden, *Phil. Trans. R. Soc. A* **359**, 997 (2001).
- [5] V. Jamali, N. Behabtu, B. Senyuk, J. A. Lee, I. I. Smalyukh, P. van der Schoot, and M. Pasquali, *Phys. Rev. E* **91**, 042507 (2015).
- [6] A. DeBenedictis and T. J. Atherton, *Liq. Cryst.* **43**, 2352 (2016).
- [7] P. G. De Gennes, *Solid State Commun.* **8**, 213 (1970).
- [8] A. Suh, M.-J. Gim, D. Beller, and D. K. Yoon, *Soft Matter* **31**, 196 (2019).
- [9] R. B. Meyer, *Mol. Cryst. Liq. Cryst.* **16**, 355 (1972).

- [10] N. Madhusudana and K. Sumathy, *Mol. Cryst. Liq. Cryst.* **92**, 193 (1983).
- [11] E. G. Virga and M. Schadt, *Jpn. J. Appl. Phys.* **39**, 6637 (2000).
- [12] E. G. Virga, *Phil. Trans. R. Soc. A* **355**, 2035 (1997).
- [13] R. Meister, H. Dumoulin, M.-A. Hallé, and P. Pieranski, *J. Phys. II* **6**, 827 (1996).
- [14] R. Eelkema, M. M. Pollard, J. Vicario, N. Katsonis, B. Serrano Ramon, C. W. M. Bastiaansen, D. J. Broer, and B. L. Feringa, *Nature (London)* **440**, 163 (2006).
- [15] M. B. Hesse, *Forces and Fields: A Concept of Action at a Distance in the History of Physics* (Dover, New York, 1962).
- [16] See Supplemental Material at [\\*http://link.aps.org/supplemental/10.1103/PhysRevLett.126.057803](http://link.aps.org/supplemental/10.1103/PhysRevLett.126.057803) for a description of the experimental details, which includes Refs. [17] and [18].
- [17] I. Gharbi, A. Missaoui, D. Demaille, E. Lacaze, and C. Rosenblatt, *Crystals* **7**, 358 (2017).
- [18] B. S. Murray, R. A. Pelcovits, and C. Rosenblatt, *Phys. Rev. E* **90**, 052501 (2014).
- [19] G. Carbone, G. Lombardo, R. Barberi, I. Musevic, and U. Tkalec, *Phys. Rev. Lett.* **103**, 167801 (2009).
- [20] Ph. Martinot-Lagarde, H. Dreyfus-Lambez, and I. Dozov, *Phys. Rev. E* **67**, 051710 (2003).
- [21] S. Kralj, B. S. Murray, and C. Rosenblatt, *Phys. Rev. E* **95**, 042702 (2017).
- [22] S. Kralj, R. Rosso, and E. G. Virga, *Phys. Rev. E* **81**, 021702 (2010).
- [23] F. Bisi, E. G. Virga, and G. E. Durand, *Phys. Rev. E* **70**, 042701 (2004).
- [24] R. Hamdi, G. Lombardo, M. P. de Santo, and R. Barberi, *Eur. Phys. J. E* **36**, 115 (2013).
- [25] P. E. Cladis and M. Kleman, *J. Phys.* **40**, 325 (1979).
- [26] C. Chiccoli, I. Feruli, O. D. Lavrentovich, P. Pasini, S. V. Shiyankovskii, and C. Zannoni, *Phys. Rev. E* **66**, 030701(R) (2002).
- [27] W. Guo, S. Herminghaus, and C. Bahr, *Langmuir* **24**, 8174 (2008).
- [28] M. A. Gharbi, I. B. Liu, Y. Luo, F. Serra, N. D. Bade, H.-N. Kim, Y. Xia, R. D. Kamien, S. Yang, and K. J. Stebe, *Langmuir* **31**, 11135 (2015).
- [29] P. G. DeGennes and J. Prost, *The Physics of Liquid Crystals* (Clarendon, Oxford 1994).
- [30] C. Rosenblatt, *Phys. Rev. Lett.* **53**, 791 (1984).
- [31] C. Rosenblatt, *J. Phys. (Paris)* **45**, 1087 (1984).
- [32] Z. Li and O. D. Lavrentovich, *Phys. Rev. Lett.* **73**, 280 (1994).
- [33] A. DeBenedictis and T. J. Atherton, *Liq. Cryst.* **43**, 2352 (2016).